QUANTUM MONTE CARLO IN THE INFINITE DIMENSIONAL LIMIT

M. Jarrell, H. Akhlaghpour and Th. Pruschke†
Department of Physics
University of Cincinnati
Cincinnati, Ohio 45221

This article has appeared in print
Quantum Monte Carlo Methods in Condensed Matter Physics
Ed. M. Suzuki, (World Scientific, 1993)

† Institut für Theoretische Physik
Universität Regensburg
93040 Regensburg, Germany

e-mail: Mark.Jarrell@uc.edu

Abstract

A new Quantum Monte Carlo algorithm is used to solve models of strongly correlated systems in the limits of infinite spatial dimensions and lattice size. A detailed description of this algorithm is given, concentrating on the methods used to reduce systematic errors and to measure the two-particle properties. The algorithm is then applied to the Hubbard model, which is shown to retain the qualitative features expected in the limit of finite dimensions. These include a Mott gap and antiferromagnetism for the half-filled model. Away from half filling the Mott gap disappears, replaced by a Kondo-like peak in the density of states associated with screening of the local spin. At low temperatures and low doping, a transition to an incommensurate magnetic states is also observed. In the paramagnetic state of the lightly doped model, we find anomalies in the resistivity and inverse NMR rate which are strikingly similar to those characteristic for the cuprate high temperature superconductors ($\rho \sim T$ and $1/T_1 \sim T$ at high temperatures).

1 Introduction

Many different materials are thought to be described by models of strongly correlated electrons. For example, The Hubbard model[1] is thought to at least qualitatively describe some of the properties of transition metal oxides, and possibly high temperature superconductors [2]; the Periodic Anderson model (PAM) seems to be the generic model for Heavy Fermion systems and the Anderson insulators; the Holstein model incorporates the essential physics of strongly interacting electrons and phonons. All of these model Hamiltonians contain at least two major ingredients: a local interaction term and a non-local hopping term. For example, for the Hubbard model reads

$$H = -\frac{t^*}{2\sqrt{d}} \sum_{\langle j,k\rangle\sigma} (c^\dagger_{j\sigma} c_{k\sigma} + c^\dagger_{k\sigma} c_{j\sigma}) + \sum_j \epsilon(n_{j\uparrow} + n_{j\downarrow}) + U(n_{j\uparrow} - 1/2)(n_{j\downarrow} - 1/2)\,, \quad (1)$$

where $c^\dagger_{j\sigma}$ ($c_{j\sigma}$) creates (destroys) an electron at site j with spin σ, $n_{i\sigma} = c^\dagger_{i\sigma} c_{i\sigma}$, and $t^* = 1$ sets our unit of energy.

However, except for special limits, even such simplified models like (1) cannot be solved exactly. For example, for the Hubbard model, no exact solution exist except in one dimension, where the knowledge is in fact rather complete [3]. The Periodic Anderson model is only solvable in the limit where the orbital degeneracy diverges[4], and the Holstein model is only solvable in the Eliashberg-Migdal limit where vertex corrections may be neglected. Clearly a new approach to these models is needed if nontrivial exact solutions are desired.

Recently, Metzner and Vollhardt suggested such a new approach [5, 6, 7] based on an expansion in $1/d$ about the point $d = \infty$ to study these strongly correlated lattice models. The main simplification of this limit is that the single-particle Green's functions $G(R, i\omega_n)$ fall off very quickly in this limit, $G(R, i\omega_n) \propto d^{R/2}$, so that nonlocal diagrams in the irreducible self energy (and two-particle irreducible vertices) may be neglected. Thus, the self energy for the single-particle Green's function and the irreducible vertex functions have no momentum dependence and are functionals of the local Green's function [5, 8]. The many-body problem may then be solved by mapping it onto an auxiliary impurity problem [9] in a time-dependent field (that mimics the hopping of an electron onto a site at time τ and off the site at a time τ'). The effective action for the impurity problem is [10]

$$S_{eff} = \sum_\sigma \int_0^\beta d\tau \int_0^\beta d\tau' c^\dagger_\sigma(\tau) G_0^{-1}(\tau - \tau') c_\sigma(\tau') + S_{int} \quad (2)$$

where G_0^{-1} is the "bare" Green's function that contains *all of the dynamical information of the other sites of the lattice* and S_{int} describes the local interactions. The interacting Green's function is determined by[10, 11]

$$G^{-1}(i\omega_n) = G_0^{-1}(i\omega_n) - \Sigma(i\omega_n), \quad (3)$$

at each Matsubara frequency $\omega_n = (2n + 1)\pi T$. The impurity problem is mapped onto the infinite-dimensional lattice by self-consistently equating the impurity Green's function with the local Green's function of the lattice

$$G(i\omega_n) = \sum_{\mathbf{k}} G(\mathbf{k}, i\omega_n) = \frac{1}{\sqrt{\pi}} \int_{-\infty}^{\infty} dy \frac{\rho(y)}{i\omega_n - \epsilon - \Sigma_n - y}\,, \quad (4)$$

where $\rho(y) = \exp(-y^2)/\sqrt{\pi}$ is the non-interacting density of states (DOS). Thus, given some way of solving the problem described by Eq. 2, the set of Eq. 2–4 form a closed nontrivial solution of correlated lattice problems in the limit $d = \infty$.

Both the local and momentum-dependent two-particle Green's functions may also be calculated with this approach. Quite generally, the two-particle propagators with the same symmetry as the lattice, and which involve no net frequency transfer, $\chi_q(i\omega_n, i\omega_m)$ are related to the corresponding local propagator $\chi_{ii}(i\omega_n, i\omega_m)$ by the following matrix form

$$\chi_q^{-1} = \chi_{q0}^{-1} + \chi_{ii}^{-1} - \chi_{ii0}^{-1} \,. \tag{5}$$

Here , χ_{q0} is the momentum dependent two-particle propagator without vertex corrections (i.e. just the simplest bubble diagram involving the fully dressed single-particle propagator). It may be calculated with the methods developed by Müller-Hartmann[6, 12] at any value of $x(\mathbf{q}) = 1/d\sum_l cos(q_l)$ which defines a set of the equivalent points in the infinite-dimensional Brillouin zone. χ_{ii0} is the local undressed two-particle propagator, which may be constructed from the local single-particle propagator, and χ_{ii} is measured in the Monte Carlo process[11], as described below.

2 Monte Carlo Algorithm

The dynamics of the impurity problem are identical to that of an impurity embedded in a host metal described by G_0 [[8]–[10],[11]].Thus, given G_0, the impurity problem may be solved by using the quantum Monte Carlo (QMC) algorithm of Hirsch and Fye[13] (an alternative derivation of this algorithm is presented in the appendix). In the QMC the problem is cast into a discrete path formalism in imaginary time, τ_l, where $\tau_l = l\Delta\tau$, $\Delta\tau = \beta/L$, and L is the number of times slices. The values of L used ranged from 40 to 160, with the largest values of L reserved for the largest values of β since the time required by the algorithm increases like L^3. Experience shows that no severe sign problem occurs in the QMC process. Since the bare Green's function G_0^{-1} in Eq. 3 is not *a priori* known, the QMC algorithm must be iterated to determine a self-consistent solution for the Green's function of the infinite-dimensional lattice. The procedure [11] is to begin with a bare Green's function G_0^{-1}, use the QMC algorithm to determine the self energy Σ, calculate the lattice Green's function from Eq. 4, and determine a new bare Green's function from Eq. 3. This process is iterated until convergence is reached.

The details of the (Hirsch-Fye[13]) impurity algorithm are reproduced in the appendix. For the remainder of this section, we will discuss the modifications necessary to apply this algorithm to the infinite-dimensional limit. The main difficulty is that the Hirsch-Fye algorithm requires an imaginary-time path integral technique which only produces data for $G(\tau)$ at a *discrete* set of points in Euclidean time $0 < \tau < \beta$; whereas, Eqs. 3–4 require either the Matsubara frequency Green's function or the corresponding self energy. This involves a numerical approximation of the integral

$$G(i\omega_n) = \int_0^\beta d\tau e^{-i\omega_n\tau} G(\tau) \,. \tag{6}$$

Fourier transforming discretely sampled data presents some well known difficulties[14]. The principle difficulty is that Nyquist's theorem tells us that above some frequency $\omega_n = 1/2\Delta\tau$, unpredictable results are produced by conventional quadrature techniques. Typically this problem is overcome by fitting the discrete data $G(\tau)$ with a smooth cubic spline, and then performing the integral on the splined data[14]. Since the integral on the splined data may be sampled on a much finer grid than the original data, this process is referred to as over sampling.

However, a problem still remains at high frequencies, since the resulting $G(i\omega_n)$ goes quickly to zero for frequencies above the Nyquist cutoff $1/2\Delta\tau$. This presents a difficulty since causality requires that

$$\lim_{\omega_n\to\infty} G(i\omega_n) \sim \frac{1}{i\omega_n}, \tag{7}$$

In order to maintain causality[15] of the Matsubara frequency Green's functions, we condition the Fourier transform with a perturbation theory result. That is, we write

$$G(i\omega_n) = G_{pt}(i\omega_n) + \int_0^\beta d\tau e^{-i\omega_n\tau}\left(G(\tau) - G_{pt}(\tau)\right) . \tag{8}$$

where G_{pt} is a Green's function obtained from perturbation theory, and the integral here is performed by the oversampling method described above.

There are two obvious advantages to this approach. First, the integral goes to zero for frequencies greater than the Nyquist frequency $1/2\Delta\tau$, so that the resulting Green's function has the same asymptotic behavior as the perturbation theory result, and is thus causal. Second, often, the perturbation theory result is asymptotically exact (i.e. results from a high temperature expansion etc.), and this then presents a way of appending exact QMC results at low frequency with asymptotically exact perturbation theory results at high frequency. The flow chart for the resulting algorithm is shown in Fig. 1.

Once convergence of the algorithm in Fig. 1 is reached, the physical properties of the system are calculated with the Monte Carlo. A variety of two-particle properties may also be calculated in the QMC approach since the irreducible vertex function is also local. For most quantities, this is straight-forward; however, the two-particle Green's functions $\chi_{ii}(i\omega_n, i\omega_m)$ are difficult to measure efficiently. For example, consider the opposite-spin particle-hole propagator

$$\chi_{ii}(i\omega_n, i\omega_m) = \int_0^\beta d\tau_1 \cdots d\tau_4 e^{[i\omega_n(\tau_1-\tau_2)-i\omega_m(\tau_3-\tau_4)]}\langle T_\tau C_\uparrow(\tau_1)C_\downarrow(\tau_2)C_\downarrow^\dagger(\tau_4)C_\uparrow^\dagger(\tau_3)\rangle . \tag{9}$$

For a particular configuration of the Hubbard-Stratonovich fields, the Fermions are noninteracting, thus the expectation value indicated by the angle brackets above may be evaluated in two steps. First, using Wick's theorem, its value is tabulated for each field configuration $\{s_l\}$. Second we Monte Carlo average over these configurations. After the first step, the equation becomes

$$\chi_{ii}(i\omega_n, i\omega_m) = \left\langle \int_0^\beta d\tau_1 \cdots d\tau_4 e^{[i\omega_n(\tau_1-\tau_2)-i\omega_m(\tau_3-\tau_4)]} g_\uparrow(\tau_4,\tau_1) g_\downarrow(\tau_3,\tau_2)\right\rangle_{m.c.} \tag{10}$$

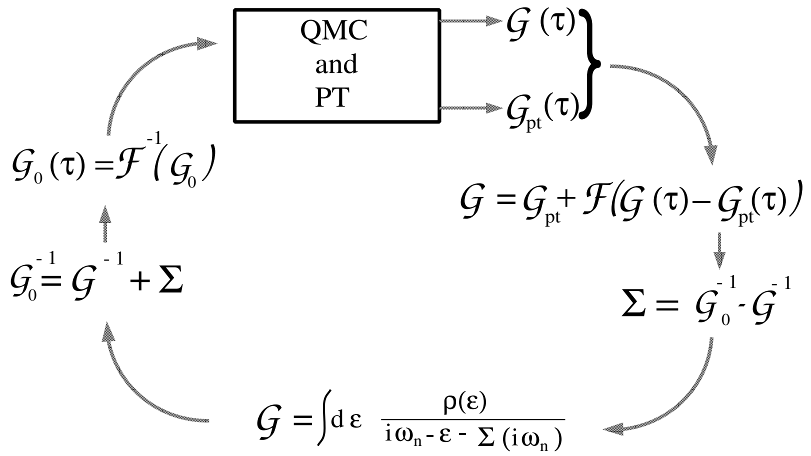

Figure 1: *Flowchart for the $d = \infty$ algorithm. The symbol $\mathcal{F}$ denote that a Fourier transform is to be performed by oversampling, and $\mathcal{F}^{-1}$ denotes its inverse.*

where the $m.c.$ subscript means that the Monte Carlo average is still to be performed.

To measure this on the computer, the integrals must be approximated by sums. Since the Green's functions change discontinuously when the two time arguments intersect, the best integral approximation that can be used here is the trapezoidal approximation. Using this, we will run into Green's functions with both time arguments the same $g(j,j)$. This is stored as $g(j^+,j)$ (i.e. it is assumed that the first time argument is slightly greater than the second), but in the sums we clearly want the equal time Green's function to be the average $\{g(j^+,j)+g(j,j^+)\}/2 = g(j^+,j)-1/2$. If we call $\mathbf{g}$, with $1/2$ subtracted from its diagonal elements, $\overline{\mathbf{g}}$, then

$$\begin{aligned}\chi_{ii}(j,k) \quad = \quad & \Bigg\langle \left(\sum_{n,n'} \Delta\tau \; e^{+i\pi n'(2j+1)} \overline{g}_{\uparrow}(n',n) \; \Delta\tau \; e^{-i\pi n'(2k+1)} \right) \\ & \left(\sum_{m,m'} \Delta\tau \; e^{-i\pi m'(2j+1)} \overline{g}_{\downarrow}(m',m) \; \Delta\tau \; e^{+i\pi m'(2k+1)} \right) \Bigg\rangle_{m.c.}\end{aligned} \tag{11}$$

This measurement may be performed efficiently if each term in parenthesis is tabulated first and stored as a matrix, and then the direct product of the two matrices taken as the estimate of χ_{ii}. When done this way, the time required for this measurement scales like $\sim L^3$ rather than $\sim L^4$ as would result from a straight-forward evaluation of the sums implicit in Eq. 10.

3 Application: The Hubbard Model

To illustrate the usefulness of this algorithm, we will apply it to the Hubbard model and show that the model in this limit retains most of the physics expected of the model in the finite-dimensional limit.

3.1 Magnetic Properties

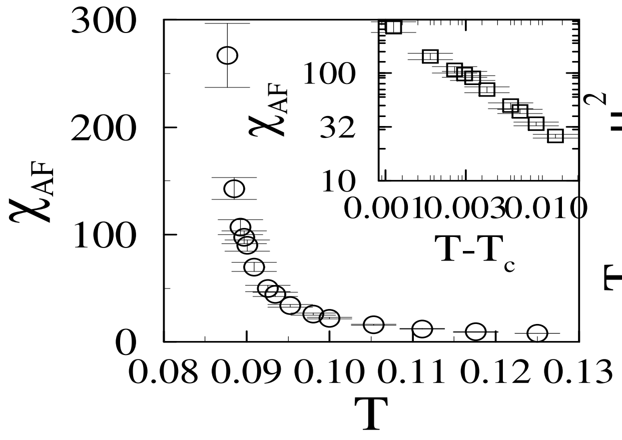

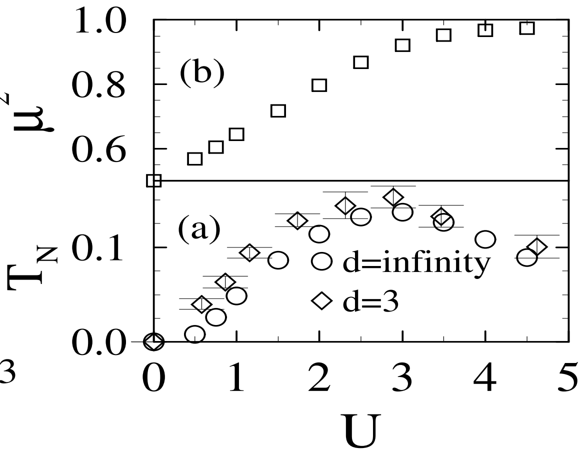

Figure 2: *LEFT: Antiferromagnetic susceptibility $\chi_{AF}(T)$, versus temperature T when $U = 1.5$ and $\epsilon = 0.0$. The logarithmic scaling behavior is shown in the inset. The data close to the transition fit the form $\chi_{AF} \propto |T - T_N|^{\nu}$ with $T_N = 0.0866 \pm 0.0003$ and $\nu = -0.99 \pm 0.05$ consistent with the mean-field behavior expected for $d = \infty$.*

Figure 3: *RIGHT: (a) Antiferromagnetic T_N and (b) $\mu^2 =< (n_\uparrow - n_\downarrow)^2 >$ (calculated at $T = T_N$) as functions of U for the half-filled model ($\epsilon = 0$). In (a) the circles represent the values obtained from the present approach while the diamonds are data for a three-dimensional Hubbard model extracted from ref.[17].*

At half filling and large U, the system can gain hybridization energy if spins on adjacent sites are antiferromagnetically aligned. Thus, as the temperature falls, antiferromagnetism is expected in the half-filled model. This is shown in Fig. 2. Furthermore, since each lattice site has an infinite number of near neighbors, we expect this transition to be mean-field-like, $\chi_{AF} \sim 1/|T - T_c|$. This behavior is illustrated in the inset. The antiferromagnetic transition temperature T_N obtained within the current approach is plotted as a function of U in Fig. 3a. For small values of U, where the local spin moment is also small, we find that T_N is exponentially small, consistent with perturbation theory [16]. For very large values of U, where the spin moment and antiferromagnetic exchange have saturated to their maximum values, one expects that the transition temperature will fall monotonically with increasing U, $T_N \sim 1/U$ [16]. This is because the net antiferromagnetic exchange $dJ \sim t^{*2}/U$ also decreases with increasing U. Thus, one expects a peak in $T_N(U)$ for some intermediate value of U as seen in Fig. 3a. For comparison we included in Fig. 3a $T_N(U)$ for the $d = 3$ Hubbard model as calculated by Scalettar et al. [17]. The shape and order of magnitude compare very well, although the $d = 3$ data always have slightly larger values. At least part of this discrepancy is a consequence of the different analytic structures of the free DOS in $d = 3$ and $d = \infty$. In Fig. 3b the unscreened squared magnetic moment $\mu^2 =< (n_\uparrow - n_\downarrow)^2 >$, calculated at the transition $T = T_N$, is plotted versus U when $\epsilon = 0$. For the half-filled model μ^2 ranges from $\mu^2 = 0.5$ in the uncorrelated limit ($U = 0$), to $\mu^2 = 1$ in the strongly correlated limit ($U \to \infty$). Note that the peak in $T_N(U)$ occurs near the point where μ^2 begins to saturate to one.

Away from half filling the transition temperature falls quickly with doping, $\delta = 1- < n >$. Once the doping exceeds a certain value, the transition is to an incommensurate state, as indicated by the divergence of the susceptibility $\chi(x(\mathbf{q}), T)$ at a value of $x > -1$. This behavior is illustrated in Fig. 4 when $U = 4$. The transition temperature may then be determined by extrapolating the inverse of the peak in the susceptibility, $1/\chi_{max}$, as shown in the inset. In Fig. 5, the corresponding transition temperatures are plotted as a function of doping. The open symbols indicate that the first divergence of the susceptibility was antiferromagnetic ($x = -1$); whereas, the filled symbols indicate that the susceptibility diverges into an incommensurate state (in the case $\delta = 0.2455$, the extrapolation lead to a negative transition temperature, indicating the lack of a transition at this doping).

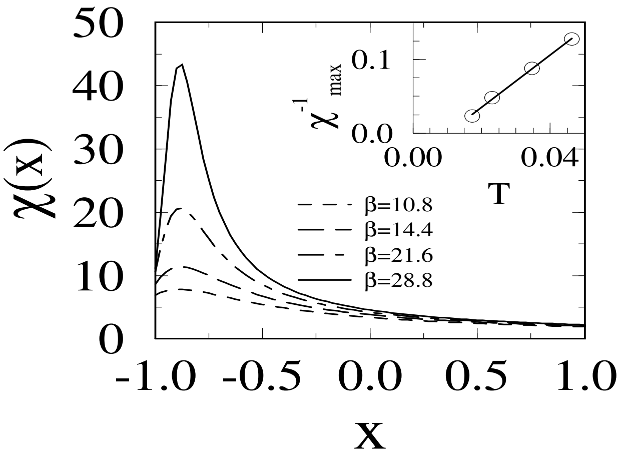

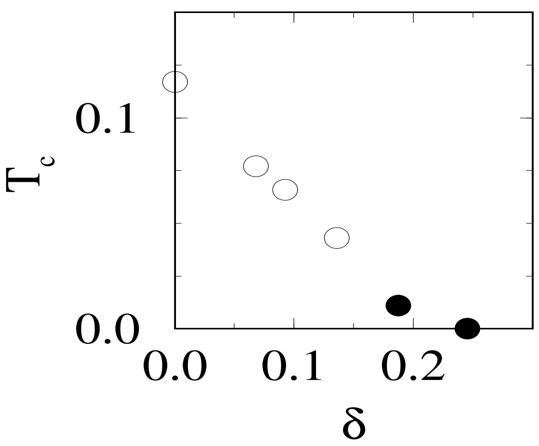

Figure 4: *LEFT: Susceptibility , $\chi(x(\mathbf{q}), T)$ versus $x(\mathbf{q}) = 1/d \sum_l cos(q_l)$ when $U = 4$ and $\delta = 0.1788$. The scaling behavior of the peak susceptibility χ_{max} is shown in the inset. The data close to the transition fit the form $1/\chi_{max} = 1/\chi(x = -0.875, T) \propto T - T_c$ with $T_c = 0.011$, consistent with the mean-field behavior expected for $d = \infty$.*

Figure 5: *RIGHT: Transition temperature T_c versus doping when $U = 4$. The open symbols indicate that the first divergence of the susceptibility was antiferromagnetic ($x = -1$); whereas, the filled symbols indicate that the susceptibility diverges into an incommensurate state. (In the case $\delta = 0.2455$, the inverse peak susceptibility extrapolated to a negative transition temperature, indicating the lack of a transition at this doping.)*

3.2 Single-Particle Density of States

In this section we will discuss the single-particle properties of the $d = \infty$ Hubbard model. The most important quantity in this connection is the single-particle density of states (DOS) defined by $N(\omega) = -1/2\pi \sum_\sigma \mathrm{Im} G_{\sigma ii}(\omega + i0^+)$. Since the QMC method supplies us only with the imaginary time Green's function $G_{ii}(\tau)$, we used the maximum entropy procedure [18, 19, 20] for providing its analytic continuation. In most cases, the finite-U non-crossing approximation[21] was used to provide a default model for this procedure. However, for Figs. 6–7, a simple ($U = 0$) Gaussian density of states was used as a default.

Above the AF transition of the half-filled model, one expects to see a correlation induced Mott-Hubbard gap for sufficiently large values of U. This is shown in Fig. 7, where $N(\omega)$ is plotted for several values of U when $\beta = 7.2$, $\epsilon = 0$, and $\delta = 0$. As the

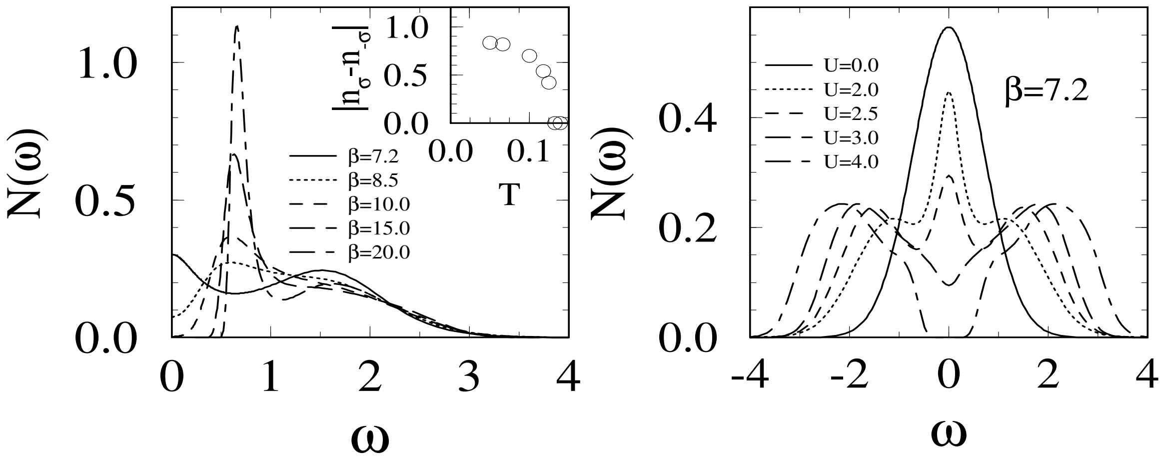

Figure 6: *LEFT: Evolution of the Neél gap in the DOS in the antiferromagnetic phase of the half-filled model when $U = 2.5$. In the inset, the ordered Neél moment is plotted versus temperature.*

Figure 7: *RIGHT: Evolution of $N(\omega)$ in the paramagnetic phase of the half-filled model for fixed inverse temperature $\beta = 7.2$.*

Coulomb repulsion U is increased from zero the broad central peak in the spectrum becomes narrower and is gradually suppressed while at the same time two side bands build up which are carrying the majority of the spectral weight. The central peak can be associated with a quasi-particle resonance, and the side peaks as usual with incoherent charge transfer on and off the site. As U continues to rise, the spectrum begins to develop a pseudogap at zero frequency when $U > 3.4 \approx U_C$. The "critical" value U_C increases with increasing temperature, and for $U > U_C$ the pseudogap grows linearly in U.

This algorithm[11] may be easily modified[22] to work below T_N in the antiferromagnetic phase of the half-filled model. As shown in Fig. 6, when $T < T_N$ a gap develops in the density of states due to the doubling of the unit cell. It is interesting to note that this gap develops continuously, so that when $T \lesssim T_N$, thermally induced states make the DOS finite at the Fermi surface. The width of this gap, measured from $\omega = 0$ to the first peak, increases monotonically with the ordered moment $|n_\downarrow - n_\uparrow|$ shown in the inset to Fig. 6.

Away from half filling, as shown in Fig. 8, the paramagnetic system becomes a heavy metal characterized by a narrow peak of width $\approx T_0$ in the single-particle density of states near the Fermi surface [23]. The development of this peak is associated with a screening of the local moments[23], as shown in the inset to Fig. 8. Hence, we associate the peak with the Kondo effect and its width T_0 with the Kondo scale. T_0 may then be determined by requiring $\chi_{ii}(T=0) = 1/T_0$[24].

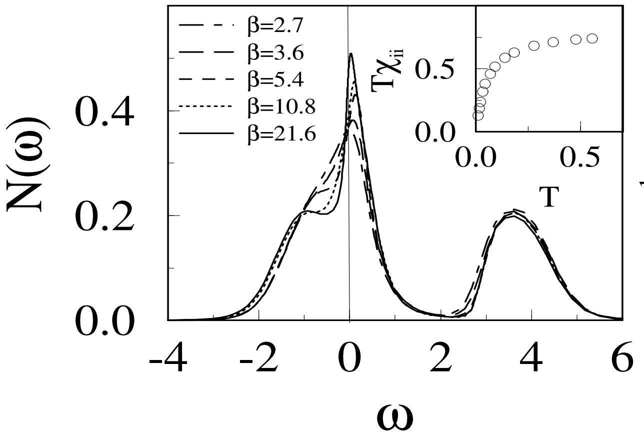

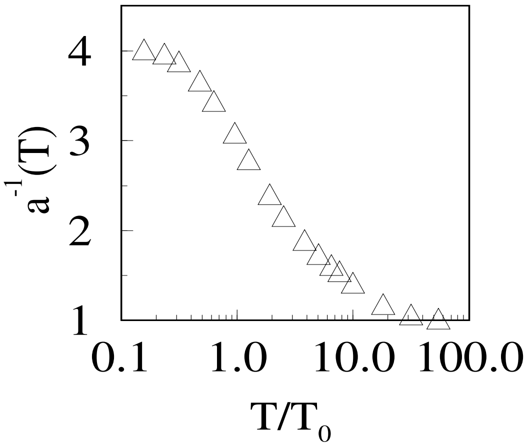

Figure 8: *LEFT: The evolution of the density of states when $U = 4$ and $\delta = 0.1878$. The development of a sharp peak at the Fermi surface is correlated with the reduction of the screened local moment $T\chi_{ii}(T)$, as shown in the inset.*

Figure 9: *RIGHT: The evolution of the finite temperature quasiparticle renormalization factor when $U = 4$ and $\delta = 0.1878$. At low temperatures, the mass enhancement $m^*/m = a^{-1}(T=0) \approx 4$*

The development of the Kondo peak is also associated with an enhancement of the effective electron mass, as shown in Fig. 9. To examine whether the low-temperature phase of the $D = \infty$ Hubbard model is a Fermi liquid or not one may calculate the finite temperature quasi-particle renormalization factor as defined by Serene and Hess[25], $a^{-1}(T) = 1 - \mathrm{Im}\Sigma(i\omega_o)/\omega_o$. In Fig. 9, the renormalization factor is plotted versus T/T_0 when $U = 4$ and $\delta = 0.1878$. Three different regions may be identified in this data: *The Fermi liquid regime, $T \ll T_0$.* As the temperature is reduced below T_0, $a^{-1}(T)$ saturates to a finite value, indicating the formation of a Fermi liquid. The zero temperature limit of $a^{-1}(T)$ may be obtained by extrapolation, and it gives the effective mass for the quasi-particles of this Fermi liquid $m^*/m = a^{-1}(0) \approx 4$. For fixed U, the effective mass appears to diverge continuously as half filling is approached[24]. *The high temperature regime, $T \gg T_0$.* The Kondo peak disappears [23] and $a^{-1}(T) \to 1$ as in the free metal. The physical properties no longer show scaling. *The crossover regime, $T \approx T_0$.* Here, $a^{-1}(T)$ increases in a roughly log-linear fashion. This behavior $a^{-1}(T) \sim \ln(T)$ has been identified [25] as a signal of marginal Fermi liquid behavior [26]. Let us stress, though, that this special behavior appears only as a crossover feature from a high- to a low-temperature regime and does not persist as an anomalous ground state!

3.3 Transport Anomalies

The Hubbard Hamiltonian [1] is usually considered the simplest model that contains at least some of the anomalous features of the high-T_c superconductors [27, 2]. These anomalies include a resistivity and the inverse NMR rate $1/T_1$ which increase linearly with temperature. We find that the infinite-dimensional Hubbard model exhibits strikingly similar anomalies.

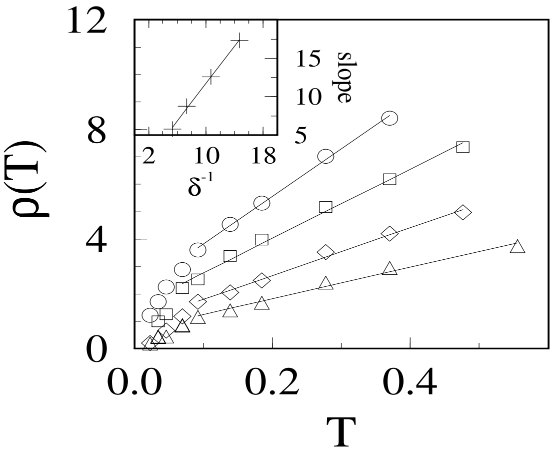

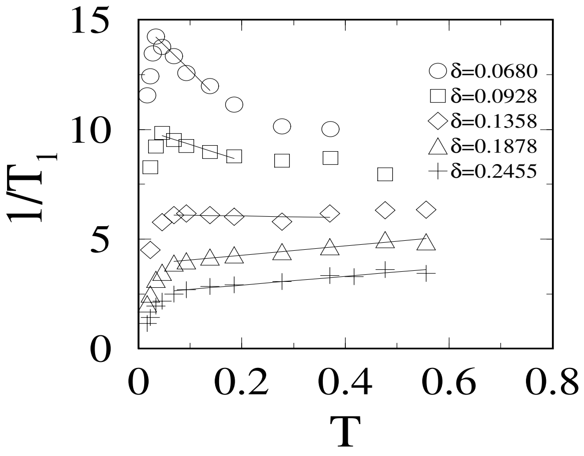

Figure 10: *LEFT: Resistivity versus temperature for several different dopings when* $U = 4$*. The lines are are linear fits to the anomalous resistivity. The slope determined by this fitting procedure increases linearly with* $1/\delta$ *as shown in the inset.*

Figure 11: *RIGHT: NMR relaxation* $1/T_1$ *vs. temperature for different dopings at* $U = 4t^*$*. The lines are linear fits to the anomalous data.*

The NMR relaxation rate $1/T_1$ is shown in Fig. 11 for several dopings vs. temperature. Remarkable is a linear region, which is most pronounced for larger dopings. The slope of this linear region shows in addition a sign change for dopings less than $\approx 15\%$. This quite anomalous behavior is also observed in the NMR data of the cuprate superconductors [28]

A similarly interesting behavior can also be found in the resistivity data collected in Fig. 10. For doping $\delta > 10\%$ one encounters a pronounced linear region, $\rho(T) \sim aT$. As shown in the inset to Fig. 10, the slope a of this linear resistivity depends on the doping δ like $a \sim \delta^{-1}$. Both results are again in agreement with experimental results for the cuprate superconductors [29]

It is interesting to speculate about the excitations responsible for these anomalies. Given that non-local dynamical correlations are suppressed in the infinite-dimensional limit, one may eliminate all excitations except local spin and charge excitations as candidates. Since the latter occur at relatively large energy scales ($\sim U$), charge fluctuations may also be eliminated, leaving only the local spin fluctuations, i. e. Kondo screening, as the scattering mechanism responsible for the transport anomalies. Transport anomalies due to Kondo screening are not unusual. They are responsible for the anomalous transport seen in dilute magnetic alloys, and heavy Fermion metals. However, since in the Hubbard model each lattice site is embedded in a band consisting only of similar correlated sites, the self consistency causes a strong normalization of the site's environment. This strong renormalization causes the transport in the Hubbard model to be different than that seen in the Periodic Anderson model.

4 Conclusion

Conventional methods of computational physics, such as QMC, are often restricted to relatively small systems, and display technical problems like the sign-problem. These difficulties make calculations and interpretations very difficult, especially in the interesting parameter regimes of low temperatures and strong electronic correlations. Our method of combining the simplifications arising in the limit of $d \to \infty$ with standard QMC techniques completely overcomes these difficulties. We are thus able to present a new approach that allows us to address consistently and (numerically) exactly physical properties of strongly correlated electron systems in a nontrivial limit over a wide range of parameters in the thermodynamic limit.

As an example, we applied this method to the single-band Hubbard model, Eq. 1. In contrast to various approximate methods, our solution shows all the expected features – an antiferromagnetically ordered ground-state close to half filling, and a metal-insulator transition at half filling – while retaining the essential dynamics induced by the local correlations. Especially this last feature led to new and unexpected results away from half filling, namely some sort of self-consistent "Kondo-effect" that yields quite anomalous transport properties.

We have also applied this method to the periodic Anderson[30] and Holstein[31] models, and demonstrated that they also retain the properties expected of their three-dimensional counterparts. We believe that this new approach represents a powerful method to solve strongly correlated lattice models and that most of our results will persist even for finite dimensionality.

We would like to acknowledge useful conversations with D.L. Cox, J. Freericks, B. Goodman, H. R. Krishnamurthy, J. Keller, M. Ma, R. Scalettar, and Matthew Steiner. This work was supported by the National Science Foundation grant number DMR-9107563, and by the Ohio Supercomputing Center. Two of the authors (MJ and TP) would also like to thank the hospitality of the Institute für Theoretische Physik of the University of Regensburg where part of this work was done.

1 Derivation of Quantum MC algorithm of Hirsch and Fye

The purpose of this section is to derive the Hirsch-Fye algorithm[13] using Grassmann algebra. We begin by splitting the Single Impurity Anderson Model (SIAM)

Hamiltonian, into bare and interacting parts, $H_{SIAM} = H_0 + H_I$, where

$$H_0 = \sum_{k,\sigma} (\epsilon_c + \epsilon_k) c^\dagger_{k,\sigma} c_{k,\sigma} + V \sum_{k,\sigma} (f^\dagger_\sigma c_{k,\sigma} + c^\dagger_{k,\sigma} f_\sigma) + \epsilon(n_\uparrow + n_\downarrow) \qquad (A1)$$

and

$$H_I = U(n_{f\uparrow} - 1/2)(n_{f\downarrow} - 1/2)\,. \qquad (A2)$$

To obtain the Trotter-Suzuki decomposition for the partition function [32] we divide the interval $[0, \beta]$ into L sufficiently small subintervals such that $\Delta\tau^2\,[H_0, H_I]$ may be neglected. This leads to

$$Z = Tre^{-\beta H} = Tr \prod_{l=1}^{L} e^{-\Delta\tau H} \approx Tr \prod_{l=1}^{L} e^{-\Delta\tau H_0} e^{-\Delta\tau H_I}\,. \qquad (A3)$$

The interacting part of the Hamiltonian may be further decoupled by mapping it to an auxiliary Ising field via a discrete Hirsch-Hubbard-Stratonovich[33] transformation,

$$e^{-\Delta\tau H_I} = e^{-\Delta\tau U (n_{f\uparrow}-1/2)(n_{f\downarrow}-1/2)} = 1/2 e^{-\Delta\tau U/4} \sum_{s=\pm 1} e^{\alpha s (n_{f\uparrow} - n_{f\downarrow})} \qquad (A4)$$

where $cosh(\alpha) = e^{\Delta\tau U/2}$. Finally, one may cast Eq. (A3) into functional-integral form by using coherent states (Grassmann variables for Fermions). If we integrate out the host Fermionic degrees of freedom $\{c_{k,\sigma}\}$, then we end up with an action analogous to Eq. 2

$$S_{eff} = (\Delta\tau V)^2 \sum_{l,l',\sigma} f^*_{\sigma,l} G_0(l,l') f_{\sigma,l'} + S_{int}\,, \qquad (A5)$$

where

$$S_{int} = \sum_{l,\sigma} -f^*_{\sigma,l}(f_{\sigma,l} - f_{\sigma,l-1}) \;+\; \Delta\tau f^*_{\sigma,l}(\epsilon_f + U/2 + \frac{\alpha}{\Delta\tau} s_l \sigma) f_{\sigma,l-1} \qquad (A6)$$

and

$$G_0^{-1}(l,l') = \frac{1}{N} \sum_{\mathbf{k}} \delta_{l,l'} - \delta_{l-1,l'}(1 - \Delta\tau\epsilon_k)\,. \qquad (A7)$$

At this point the correspondence of the SIAM and the infinite-dimensional Hubbard model is clear. In both, G_0 contains the information about the host into which the impurity is embedded. The difference is that G_0 must be determined self-consistently for the lattice model.

We will now proceed to derive the Monte Carlo algorithm[13] sufficient for either the SIAM or the infinite-dimensional lattice problem. By integrating over $f_{\sigma,l}$ we can write down the partition function (neglecting a numerical prefactor), as

$$Z = \sum_{\{s_l\}} det(G^{-1}_{\uparrow\{s_l\}}) det(G^{-1}_{\downarrow\{s_l\}}) \qquad (A8)$$

where

$$G^{-1}_{\sigma,\{s_l\}}(l,l') = \delta_{l,l'} - \delta_{l-1,l'}(1-\Delta\tau\epsilon_f + \alpha s_l\sigma) - \Delta\tau^2 V^2 G_0(l,l') \qquad (A9)$$

and we sum over all configurations of Hubbard-Stratonovich field $\{s_l\}$. If we reexponentiate the above formula by defining $\mathcal{V}_{\sigma,\{s_l\}}(l) \equiv \Delta\tau(\epsilon_f + \alpha s_l\sigma/\Delta\tau)$, we can write it in a simple notation as

$$G^{-1}_\sigma = 1 + Te^{\mathcal{V}_\sigma} + \Delta\tau^2 V^2 G_0 \ ,$$

where T is $\delta_{l-1,l'}$ and $\mathcal{V}_\sigma \equiv \mathcal{V}_{\sigma,\{s_l\}}(l)$ for one special configuration. For another field configuration the only difference comes from $\mathcal{V}_\sigma$ such that $G'^{-1}_\sigma - G^{-1}_\sigma = T(e^{\mathcal{V}'_\sigma} - e^{\mathcal{V}_\sigma}) + O(\Delta\tau^{3/2})$ (note that α is of the order of $\Delta\tau^{1/2}$). On the other hand $T = (G^{-1}_\sigma - 1 - \Delta\tau^2V^2G_0)e^{-\mathcal{V}_\sigma}$ which results

$$G'^{-1}_\sigma - G^{-1}_\sigma = (G^{-1}_\sigma - 1)e^{-\mathcal{V}_\sigma}(e^{\mathcal{V}'_\sigma} - e^{\mathcal{V}_\sigma}) + O(\Delta\tau^{3/2})\,. \qquad (A10)$$

Multiplying from the left by G and from the right by G' and, ignoring terms $O(\Delta\tau^{3/2})$, we find

$$G'_\sigma = G_\sigma + (G_\sigma - 1)(e^{\mathcal{V}'_\sigma - \mathcal{V}_\sigma} - 1)G'_\sigma \ or \ G_\sigma G'^{-1}_\sigma = 1 + (1-G_\sigma)(e^{\mathcal{V}'_\sigma - \mathcal{V}_\sigma} - 1) \quad (A11)$$

The probability of having a configuration $\{s_l\}$ is $P_s \propto det(G^{-1}_{\uparrow\{s_l\}})det(G^{-1}_{\downarrow\{s_l\}})$; on the other hand the detailed balance requires $P_{s'}P_{s'->s} = P_sP_{s->s'}$ for all s'. We may satisfy this requirement by defining the probability of going from $\{s_l\}$ to $\{s'_l\}$ as $R/(1+R)$, where

$$R \equiv \frac{det(G'_\uparrow)det(G'_\downarrow)}{det(G_\uparrow)det(G_\downarrow)} \qquad (A12)$$

is the relative weight of two configurations. If the difference between two configuration is due to a flip of a single Hubbard Stratonovich field at the mth imaginary time slice then[13]

$$R = \prod_\sigma [1 + (1 - G_{\sigma m,m})(e^{-2\alpha\sigma s_m} - 1)]^{-1}\,. \qquad (A13)$$

Finally we can write down the evolution of the Green's function in the QMC time as[13]

$$G'_{\sigma i,j} = G_{\sigma i,j} + (G_{\sigma i,m} - \delta_{i,m}) \times (e^{-2\alpha\sigma s_m} - 1)\{1 + (1 - G_{\sigma m,m})(e^{-2\alpha\sigma s_m} - 1)\}^{-1} G_{\sigma m,j}\,. \qquad (A14)$$

The QMC process precedes by sequentially proposing changes in each spin, accepting these changes with probability $P_{s->s'}$, and updating the Greens function with Eq. A14 when the change is accepted.

References

1. J. Hubbard, Proc. R. Soc. a**276**, 238(1963); M.C. Gutzwiller, Phys. Rev. Lett. **10**, 159(1963); J. Kanamori, Prog. Theor. Phys. **30**, 257(1963).

2. Proceedings of the international conference on "Itinerant-Electron Magnetism". Physica B+C**91** (1977); for a review about the theory of the Hubbard model see also D. Vollhardt, Rev. Mod. Phys. 56, 99(1984).
3. E.H. Lieb and F.Y. Wu, Phys. Rev. Lett. **20**, 1445 (1968); H. Frahm nd V.E. Korepin, Phys. Rev. B**42**, 10533(1990); N. Kawakami and S.-K. Yang, Phys. Rev. Lett. **65**, 2309(1990).
4. G. Czycholl, J. Mag. Mag. Mat. **47,48**, 350 (1985).
5. W. Metzner and D Vollhardt, Phys. Rev. Lett. **62**, 324 (1989).
6. E. Müller-Hartmann, Z. Phys. B **74**, 507 (1989).
7. P.G.J. van Dongen and D. Vollhardt, Phys. Rev. Lett. **65**, 1663 (1990).
8. H. Schweitzer and G. Czycholl, Z. Phys. B **77**, 327 (1990).
9. U. Brandt and Ch. Mielsch, Z. Phys. B**75**, 365(1989); **79**, 295(1990).
10. A. Georges and G. Kotliar, Phys. Rev. **B45**,
11. M. Jarrell Phys. Rev. Lett. **69**, 168(1992).
12. E. Müller-Hartmann, Z. Phys. **B76**, 216(1989).
13. J.E. Hirsch and R.M. Fye, Phys. Rev. Lett. **56**, 2521 (1986).
14. W. H. Press, B. P. Flannery, S. A. Teukolsky, and W. T. Vetterling, *Numerical Recipes* (Cambridge University Press, Cambridge, 1986).
15. Obeying causality is crucial when Bayesian methods are used to analytically continue QMC data, since the form of the Bayesian prior is dictated by causality.
16. P.G.J. van Dongen, Phys. Rev. Lett. **67**, 757 (1991).
17. R.T. Scalettar, D.J. Scalapino, R.L. Sugar and D. Toussaint, Phys. Rev. **B39**, 4711(1989).
18. J.E. Gubernatis et al., Phys. Rev. B **44**, 6011 (1991).
19. R.K. Bryan, Eur. Biophys. J. **18**,165 (1990).
20. R.N. Silver et al., Phys. Rev. B, **41**, 2380 (1989).
21. Th. Pruschke, D.L. Cox and M. Jarrell, Phys. Rev. B. **47**, 3553 (15 Feb. 1993).
22. A. George, G. Kotliar and Q. Si, Int. Jou. of Mod. Phys. **6**, 705(1992).
23. M. Jarrell and Th. Pruschke, Z. Phys. B. **90**, 187(1993).
24. M. Jarrell and Th. Pruschke, submitted for publication.
25. J.W. Serene and D.W. Hess, Phys. Rev. **B44**, 3391(1991).
26. C.M. Varma, P.B. Littlewood, S. Schmitt-Rink, E. Abrahams and A.E. Ruckenstein, Phys. Rev. Lett. **63**, 1996(1989).
27. J.G. Bednorz and K.A. Müller, Z. Phys. **64**, 189(1986).
28. T. Imai et al., Physica C **162-164**, 169 (1989); T. Imai, C. P. Slichter, A. P. Paulikas, and B. Veal, preprint.
29. H. Takagi et al. Phys. Rev. Lett. **69**, 2975(1992); Cristoph Quitmann, Thesis RWTH Aachen.
30. M. Jarrell, H. Akhlaghpour, and Th. Pruschke, Phys. Rev. Lett. **70**, 1670 (1993).
31. J. K. Freericks, M. Jarrell, and D. J. Scalapino. Phys. Rev. B, in print.
32. H. F. Trotter, Proc. Am. Math. Soc. **10** 545 (1959); M. Suzuki, Prog. Theor. Phys. **56**, 1454 (1976)
33. J.E. Hirsch,Phys. Rev. B, **28**, 4059(1983), and **31**, 4403(1985).